ELSEVIER

Chemical Geology 242 (2007) 176–186

CHEMICAL GEOLOGY
INCLUDING
ISOTOPE GEOSCIENCE

www.elsevier.com/locate/chemgeo

Titanium substitution mechanisms in forsterite

Andrew J. Berry [a,*], Andrew M. Walker [b], Jörg Hermann [c], Hugh St.C. O'Neill [c], Garry J. Foran [d,e], Julian D. Gale [f]

[a] *Department of Earth Science and Engineering, Imperial College London, South Kensington, London, SW7 2AZ, United Kingdom*
[b] *Department of Earth Sciences, University of Cambridge, Downing Street, Cambridge, CB2 3EQ, United Kingdom*
[c] *Research School of Earth Sciences, Australian National University, Canberra, ACT 0200, Australia*
[d] *Australian Synchrotron Research Program, Australian Nuclear Science and Technology Organisation, PMB 1, Menai, NSW 2234, Australia*
[e] *Australian National Beamline Facility, KEK, Photon Factory, Oho 1-1, Tsukuba-shi, Ibaraki-ken 305-0801, Japan*
[f] *Nanochemistry Research Institute, Department of Applied Chemistry, Curtin University of Technology, P.O. Box U1987, Perth, WA 6845, Australia*

Received 30 November 2006; accepted 11 March 2007

Editor: S.L. Goldstein

Abstract

Ti K-edge X-ray absorption near edge structure (XANES) and extended X-ray absorption fine structure (EXAFS) spectra, together with atomic scale calculations, indicate that Ti occupies the Si site in anhydrous forsterite. The energy and intensity of the $1s \rightarrow 3d$ transition in the XANES spectrum is diagnostic of Ti on a four-coordinate site. The EXAFS spectra determine a Ti–O bond length of 1.81 ± 0.01 Å. This value is in excellent agreement with that of 1.8 Å determined computationally by periodic density functional theory and an embedded cluster approach for Ti on the Si site; the calculated bond length for Ti on a Mg site is 2.0 Å. Both computational methods further find that the direct substitution of Ti for Si is energetically favoured relative to substitution of Ti for Mg, charge balanced by either a Mg vacancy or Mg on a Si site. Together the results provide unambiguous evidence for Ti occupying the Si site in anhydrous forsterite. Ti-bearing olivine synthesised at upper mantle conditions in the presence of water, however, exhibits a pre-edge feature corresponding to six-fold coordination. This is consistent with the identification of a Ti-clinohumite-like point defect in samples of olivine from upper-mantle spinel peridotite. The change in Ti site thus provides a mechanism for the incorporation of water in olivine. The total Ti content of olivine will comprise varying contributions from $Mg_2^{[4]}TiO_4$ and Ti-clinohumite-like $Mg^{[6]}TiO_2(OH)_2$ substitutions.

Keywords: Forsterite; XANES; Density functional theory; EXAFS; Nominally anhydrous minerals; Hydrous defects

1. Introduction

Titanium in the 4+ oxidation state occupies an octahedral site in Ti-rich minerals such as rutile, ilmenite and titanite. Similarly, Ti occupies octahedral sites when it substitutes as a minor component into rock forming minerals, such as pyroxenes, garnets, amphiboles and micas (Waychunas, 1987). In cases where there is a stoichiometric deficiency of Si it appears that Al^{3+} and Fe^{3+} occupy tetrahedral sites preferentially to Ti^{4+} (Hartman, 1969). In the spinel group of minerals, Ti^{4+} is

* Corresponding author. Tel.: +44 207 594 7402; fax:+44 207 594 7444.
E-mail address: a.berry@imperial.ac.uk (A.J. Berry).

0009-2541/$ - see front matter © 2007 Published by Elsevier B.V.
doi:10.1016/j.chemgeo.2007.03.010

found predominantly in the octahedral site, forming inverse spinels with the cation arrangement $^{[4]}(M^{2+})^{[6]}(M^{2+}Ti^{4+})O_4$ (O'Neill and Navrotsky, 1983). While Ti can occur in [4] and [5] fold coordination, this is uncommon and usually restricted to synthetic materials (Farges et al., 1996).

There has been recent interest in the solubility of Ti in olivine because high Ti contents, inferred from the presence of ilmenite exsolutions, have been interpreted to be indicative of an ultra-deep origin (Dobrzhinetskaya et al., 1996; Green et al., 1997). It has now been established that pressure has no effect on Ti content (it actually should decrease solubility) and that for a given paragenesis temperature is the controlling factor; Ti solubility increases strongly with increasing temperature (Hermann et al., 2005). At a given temperature, the maximum Ti solubility in Mg_2SiO_4 is obtained when buffered with the spinel Mg_2TiO_4, which suggests that Ti substitutes for Si in olivine (Hermann et al., 2005). This is further supported by a negative correlation between Ti and Si contents and the absence of a correlation between Ti and Mg. For Ti substitution as an M_2TiO_4 component, exsolution arising from cooling and Ti saturation should produce spinel rather than the observed $MTiO_3$ ilmenite. This, together with the amount of Ti in some exsolution-free olivines being greater than the saturation level determined in anhydrous experiments, suggests that Ti may be incorporated at an additional site. In particular, Ti-clinohumite-like planar defects ($M^{[6]}TiO_2(OH)_2$) have been identified by transmission electron microscopy (Hermann et al., 2007; Mosenfelder et al., 2006; Kitamura et al., 1987). The total Ti content in olivine may hence comprise both anhydrous $M_2^{[4]}TiO_4$ and hydrous $M^{[6]}TiO_2(OH)_2$ components, with dehydration of $MTiO_2(OH)_2$ producing the ilmenite lamellae (Risold et al., 2001). This possible change in Ti site with hydration would provide a mechanism for the incorporation of water in mantle olivine. Indeed, recent experiments have shown that the infrared signature of the most common mode of water incorporation in spinel peridotite olivine can only be reproduced in a Ti-bearing system (Berry et al., 2005). The Ti site in olivine is therefore important for understanding Ti solubility, the exsolution of ilmenite, and water storage in the mantle.

The coordination of Ti can be determined from K-edge X-ray absorption near edge structure (XANES) spectroscopy. The spectra exhibit a pre-edge feature assigned to the $1s \rightarrow 3d$ transition (Waychunas, 1987; Dingwell et al., 1994; Farges et al., 1996). This bound state transition is forbidden in octahedral coordination, but may gain intensity in low symmetry environments through mixing of p states (to which transitions are electric dipole allowed) into the d orbitals. The pre-edge peak intensity was found to be linearly correlated with the Ti coordination number for various reference materials (Dingwell et al., 1994), and was used to infer the average coordination of Ti in glasses (Paris et al., 1994). The pre-edge transition also increases in energy with increasing coordination number and a plot of peak height versus energy defines distinct domains corresponding to Ti with [4], [5], and [6] coordination (Farges et al., 1996). This provides a simple and efficient way of accurately determining the coordination number (and hence site) of Ti in a material and is particularly useful for identifying mixed environments, such as found in glasses (Farges and Brown, 1997). Extended X-ray absorption fine structure (EXAFS) spectroscopy allows Ti–O bond lengths to be determined and provides further experimental evidence for the site occupied by Ti.

The site a trace element occupies in a crystal can also be identified by computer simulation of the response of the crystal structure to the presence of the impurity. Such a simulation, which can be performed using parameterised models of the interaction between atoms or by an approximate solution to the Schrödinger equation to give the electronic structure, provides full details of the atomic scale reconstruction around the impurity atom as well as the relative energies of the different possible mechanisms by which the impurity can be accommodated into the crystal structure. The general approach is to calculate the energy of incorporation of the impurity ion by all possible atomic scale mechanisms. The mechanism that yields the lowest energy is then the one that the computational method predicts will dominate. Coupling such an atomic scale approach with an experimental probe of the local coordination structure, such as that provided by EXAFS, is a useful combination since the prediction of the deformed structure of the crystal around the impurity can be directly compared with the experimental results.

Here we report Ti K-edge XANES and EXAFS spectra for forsterite containing up to 0.65 wt% TiO_2 and electronic structure calculations of the lowest energy Ti substitution. Together these provide unambiguous evidence that Ti occurs on the Si site in anhydrous forsterite.

2. Experimental

Ti-bearing Mg_2SiO_4 was prepared from stoichiometric amounts of MgO, SiO_2, and Ti-doped SiO_2 prepared from a fired gel of $Si(OC_2H_5)_4$ and $Ti(OC_2H_5)_4$ mixed in

a ratio to give $Si_{0.99}Ti_{0.01}O_2$. The gel method ensures a homogeneous distribution of Ti in the sample. The starting materials were pressed into a pellet and fired at 1400 °C for 24 h. A number of samples were prepared with various TiO_2 contents. Hydrous forsterite was synthesised at 1400 °C and either 15 or 25 kbar for 72 h in a Pt capsule using a piston–cylinder apparatus, from a mixture of SiO_2, MgO, $Mg(OH)_2$, and TiO_2, corresponding to 58% forsterite, 24% orthopyroxene, 15% rutile, and 3% H_2O. The pellets and sectioned capsules were mounted in epoxy, polished, and viewed by back-scattered electron (BSE) imaging using a JEOL 6400 SEM. The Ti contents were determined with a Cameca Camebax electron microprobe using an acceleration voltage of 25 kV and a beam current of 30 nA. $Ni_{2.62}Ti_{0.69}O_4$ spinel, in which Ti is tetrahedrally coordinated (prepared using the method of Lager et al., 1981), and natural ilmenite (54 wt% TiO_2; origin unknown), Ti-clinohumite (5 wt% TiO_2; Val Malenco, Italy), and Ti-andradite garnet (8 wt% TiO_2; Val Malenco, Italy), which all contain six-coordinated Ti, were used as standards. The standards were powdered, diluted with either BN (spinel 1:13; ilmenite 1:50; Ti-andradite 1:9) or olivine from San Carlos, Arizona (Ti-clinohumite 1:9), and pressed into pellets for the XANES experiments. The forsterite samples were analysed as prepared for the electron microprobe.

Ti K-edge XANES spectra were recorded in fluorescence mode at the Australian National Beamline Facility; Beamline 20B (bending magnet) at the 2.5 GeV Photon Factory (KEK, Tsukuba, Japan). The excitation energy was selected using a water-cooled Si(111) channel cut crystal monochromator, detuned 50% to reject high energy harmonics. The beam size of 2 mm (horizontal) × 1 mm (vertical) was controlled with a slit assembly 13 m from the source. The resulting energy bandpass is 1.52 eV at the Ti K edge, which when coupled with the Ti Kα core-hole width of 0.94 eV (Krause and Oliver, 1979), indicates a spectral energy resolution of 1.8 eV. The energy was calibrated by defining the first derivative peak of Ti foil to be 4996.4 eV. Fluorescence was measured at 45° to the sample, and perpendicular to the incident beam, using a Canberra GL0110S ten element Ge array detector. The signal from each array element was passed from the detector, *via* a Canberra Model 2026XA Spectroscopy Amplifier (shaping time 0.25 μs), to a Canberra Model 2030 Single Channel Analyser which was set to pass the Ti Kα signal to the counting electronics. The distance of the detector from the sample was set so as to limit the total incoming count rate to within the linear response range of the detector system. XANES spectra were recorded from 4955–5200 eV, using a step size of 0.2 eV from 4955–5015 eV and 0.25 eV above 5015 eV.

EXAFS spectra were recorded from 4765–5770 eV, using a step size of 10 eV from 4765–4965 eV (pre-edge region), a step of 0.25 eV from 4965–5025 eV (XANES region), and 0.05 Å - 1 steps in k space from 5025–5770 eV (EXAFS region). Four replicate spectra were recorded, each with an average scan time of around 90 min. The spectra were averaged, background subtracted, and modelled using the XFIT software package (Ellis and Freeman, 1995) and FEFF 4.06 (de Leon et al., 1991). The EXAFS were fit with a single-scattering shell model using the defect structure determined by density functional theory (DFT) for the initial shell distances. The fit to the experimental data was performed by a Levenberg–Marquardt algorithm within XFIT. The random errors in the calculated parameters, arising from the noise in the data, were determined by Monte Carlo analysis.

Two approaches were taken to calculate the structure and energies of possible Ti defects in forsterite. Firstly, calculations based on DFT (Hohenberg and Kohn, 1964; Kohn and Sham, 1965) were used for the examination of neutral clusters of defects within a periodic supercell. Secondly, isolated charged and charge neutral defects were examined using an embedded cluster method where the defect and its immediate surroundings are described by either the Hartree–Fock approximation or DFT, with this model being embedded in an atomistic representation of the infinite crystal.

For the periodic DFT calculations we employ the SIESTA methodology (Soler et al., 2002) where only the valence electrons, and appropriate semi-core states, are considered. The potential due to the core electrons and nucleus of the atoms is described by non-local pseudopotential projectors of the Kleinmann–Bylander form, according to the scheme of Troullier and Martins (1991), with the local component being chosen to maximise smoothness. The basis functions used to describe the valence orbitals consist of pseudo-atomic orbitals that are confined within a smooth potential that becomes asymptotic to infinity at a given radius (Junquera et al., 2001). For all species, the basis set is of double-zeta polarized (DZP) quality. The parameters that define the shape of the orbitals, such as the atomic charge state and the confinement potential radius and exponent, have been taken from previous work in which they were optimized with respect to the energy of minerals where the ions adopt similar environments as in forsterite (Junquera et al., 2001).

All calculations were performed within the Generalized Gradient Approximation (GGA), using the

functional of Perdew et al., 1996. An auxiliary basis set is employed to compute the exchange-correlation and Hartree energies, consisting of a uniform real space grid. In order to yield sufficient numerical convergence a kinetic energy cut-off of 250 Ry and 2×2×2 grid cell sampling was used.

In order to consider the defect energetics at a reasonable dilution, a 2×1×2 supercell of forsterite containing 112 atoms was employed. This yields a unit cell in which the smallest dimension is approximately 9.6 Å. In addition to performing calculations on the perfect and defective forsterite system, the optimized structures and energies of MgO, α-quartz and rutile were also determined in order to compute the full thermodynamic cycle for all equilibria. For the calculations on the bulk phases, Monkhorst–Pack mesh sizes of 6×6×6, 5×5×5 and 6×6×9 were utilized for MgO, α-quartz and rutile, respectively. In the case of the forsterite 2×1×2 supercell reciprocal space was sampled only at the gamma point. While this leads to total energies that are not absolutely converged, the error in the energy differences is found to be less than 0.01 eV and therefore not significant with respect to thermal energy or the inherent uncertainties underlying DFT.

Embedded cluster calculations were undertaken using the GUESS code (Sushko et al., 2000a,b) and the methodology used previously for studies of intrinsic and hydrous point defects in forsterite (Braithwaite et al., 2002, 2003). The methodology combines a small cluster of atoms surrounding the defect that are treated using the quantum chemical techniques implemented within the GAUSSIAN package (Frisch et al., 1998) and a larger region of the crystal described using an interatomic potential model. These two sub-systems are directly linked and the total energy of the system is expressed as the sum of the energy of the quantum mechanically treated cluster (the QM cluster) in the electrostatic field of the crystal, the electrostatic and parameterised short range interactions between atoms surrounding the QM cluster, and parameterised interactions between the surrounding atoms and a classical representation of the atoms in the QM cluster.

The parameterised model and simulation cell setup are identical to those used by Braithwaite et al. (2003). Briefly, two types of QM clusters were used; small clusters consisting of either 42 or 43 atoms centred on the M1 site were utilised to evaluate the energies of the M1 vacancy and of Ti substituting for Mg on the M1 site, respectively. Larger 96 or 97 atom clusters were used for simulations of the Si vacancy and Ti substitution onto the Si site, respectively. Both of these clusters are embedded in an identical environment of a spherical nanocluster of classical ions with a radius of 30 Å. This nanocluster is built of charge neutral units in order to give a constant electrostatic potential across the centre of the model and minimise the dipole across the cluster. When the smaller QM clusters are used all atoms in the inner 12 Å are permitted to move during the geometry optimisation. For the larger clusters, atoms within 14 Å of the defect are permitted to move.

Both of the QM clusters were treated using two different approximations to the many-electron Schrödinger equation; the Hartree–Fock approximation, with exact exchange and no correlation, and DFT with the PW91 GGA exchange and correlation functional (Perdew, 1991; Perdew and Wang, 1992). In both cases, a 6–31G basis set was used for geometry optimisation and the higher quality 6–31+G* basis was used for the calculation of the energy of the system at this optimised geometry. Convergence tests for the smaller of the two clusters show that the defect energy (energy to form the defect from isolated ions) is well converged (to within 0.1 eV) with this basis set. Computational constraints prevent more flexible basis sets being used with the larger QM cluster. In addition, for the smaller M1 centred cell, increasing the size of the basis used for geometry optimisation does not change the bond lengths by more than 0.02 Å. Although this method allows the energies of isolated point defects to be calculated, the energy of the perfect, defect free, materials can not be determined with this basis set (and attempts to modify the basis lead to large energy errors, Braithwaite et al., 2002). Instead, we restrict ourselves to an analysis of differences in defect energies and the structure of the defects.

3. Results

Back scattered electron images indicate that the anhydrous Ti-bearing forsterite samples are polycrystalline with a grain size of ~50 μm, and essentially pure, with there being no evidence of any Ti-rich phases. The TiO_2 content of two samples was determined to be 0.35 and 0.65 wt%. In previous work on similar samples the forsterite unit cell volume was found to systematically increase with the Ti content of the sample indicating the substitution of Ti into the structure rather than it being present as sub-microscopic inclusions of a Ti-rich phase (Hermann et al., 2005). Both hydrous experiments produced a number of large (~500 μm), randomly oriented forsterite crystals containing 0.11 wt% TiO_2, and hydrous melt, which was masked with Pb tape during the XANES experiments. The Ti contents are lower than those of the samples prepared at atmospheric pressure

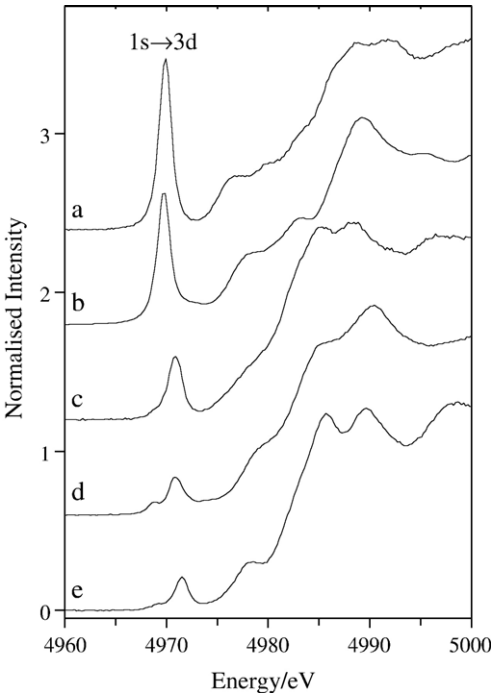

Fig. 1. Ti K-edge XANES spectra of (a) forsterite containing 0.35 wt% TiO_2, (b) $Ni_{2.6}Ti_{0.7}O_4$ spinel, (c) Ti-clinohumite, (d) ilmenite, and (e) garnet. The feature attributed to the 1s→3d pre-edge transition is indicated. Spectra are offset for clarity.

due to the presence of the hydrous melt into which Ti preferentially partitions. It was noted that the cathodoluminescence (observed with the electron microprobe) of Ti-bearing anhydrous forsterite is blue while that of the hydrous samples is yellow. These colours were consistently observed for a wide range of forsterite samples (not reported here) and appear to be diagnostic of the Ti coordination and/or hydration.

XANES spectra for the 0.35 wt% sample and standards are shown in Fig. 1. For all spectra a constant baseline was subtracted followed by normalisation to the average absorption coefficient above 5050 eV. The maximum intensity (or height) of the $1s \rightarrow 3d$ pre-edge peak in the normalised spectrum, and the energy at which it occurs, is plotted for each sample in Fig. 2, together with the values reported in Farges et al. (1996) for various reference materials. The points corresponding to the standards recorded in the present study (one with $^{[4]}$Ti and three with $^{[6]}$Ti) plot within the expected fields defined by the literature results. The pre-edge feature of the anhydrous forsterite is more intense than any other reported material and clearly indicates occupancy of a [4] site. The pre-edge intensity of hydrated forsterite synthesised at both 15 and 25 kbars is significantly reduced from that of the anhydrous samples (Fig. 3). The point for the 25 kbar sample plots unambiguously within the $^{[6]}$Ti field. The results for the 15 kbar sample, however, do not overlap within any of the defined fields but are instead close to a mixing line between the anhydrous and 25 kbar hydrous samples (Fig. 2). The line illustrates how the pre-edge intensity and energy would vary for a physical mixture of the two end members, determined from simulated spectra, and is in agreement with a similar trend determined by Farges et al. (1996) for a binary mixture of $^{[4]}$Ti and $^{[6]}$Ti oxides. The mixing line suggests that the Ti coordination in the 15 kbar sample is 10–20% $^{[4]}$Ti and 80–90% $^{[6]}$Ti.

The observed and calculated EXAFS and Fourier transform (FT) spectra of anhydrous forsterite containing 0.35 wt% TiO_2 are shown in Fig. 4. A large number of models were used to fit the EXAFS data, including Ti on the Si, M1, and M2 sites, single and multiple scattering, and windowing to fit either the total or only first shell scattering. In all cases, the first shell Ti–O bond distance was found to be ~1.804 Å, with a variability of ±0.003. This bond length determination is a robust result. To fit the contribution of the outer shells the starting distances were taken from the results of the SIESTA calculation of Ti substituting for Si. This provides relaxed distances that take into account the

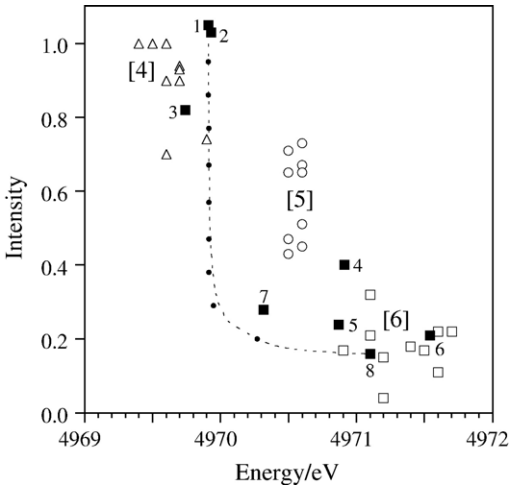

Fig. 2. Intensity versus energy of the 1s→3d pre-edge feature in Ti K-edge XANES spectra. The open symbols correspond to data from Farges et al. (1996) for model compounds which define domains for [4], [5], and [6] coordinated Ti. The solid symbols are for the present study and correspond to (1) forsterite containing 0.35 wt% TiO_2, (2) forsterite containing 0.65 wt% TiO_2, (3) $Ni_{2.6}Ti_{0.7}O_4$ spinel, (4) Ti-clinohumite, (5) ilmenite, (6) garnet, and Ti-bearing hydrous forsterite synthesised at 1400 °C and (7) 15 kbar, and (8) 25 kbar. The dashed line is the trend expected for physical mixtures of (1) and (8) where the points correspond to 10% increments.

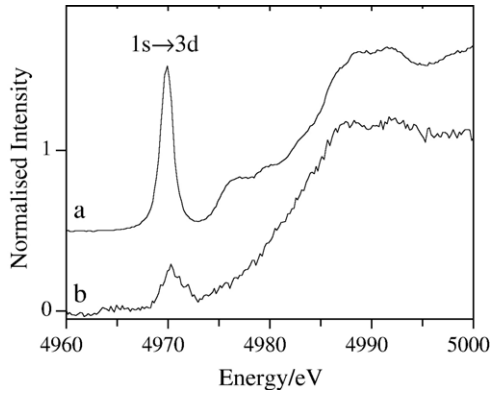

Fig. 3. Ti K-edge XANES spectra of (a) forsterite containing 0.65 wt% TiO_2 and (b) hydrated forsterite synthesised at 15 kbar (0.11 wt% TiO_2). The 1s→3d feature is indicated.

effect of the defect on the local lattice environment. In this model the number of atoms comprising each shell was fixed (except for the first shell), with only the distances and Debye–Waller factors being allowed to vary (within constraints). The variation from the starting distances was effectively insignificant. The occupancy of the first shell (highly correlated with the scale factor) is larger than expected (4.5) but well within typical uncertainties. Full details of the model are given in Table 1. EXAFS spectra could not be recorded from the hydrous samples, at the beamline used for this study, due to the comparatively low Ti contents and reduced sample size.

The energy of the simple substitution of Ti for Si, the substitution of Ti for Mg charge balanced by a vacancy on an adjacent Mg site, and the coupled substitution of Ti for Mg and Mg for Si where the two defects occupy adjacent sites were calculated using periodic DFT. Taking the point and translational symmetry into account there are 16 different ways to perform these substitutions. There are five distinct ways for Ti to occupy a Mg site adjacent to a vacant M2 site. The Ti

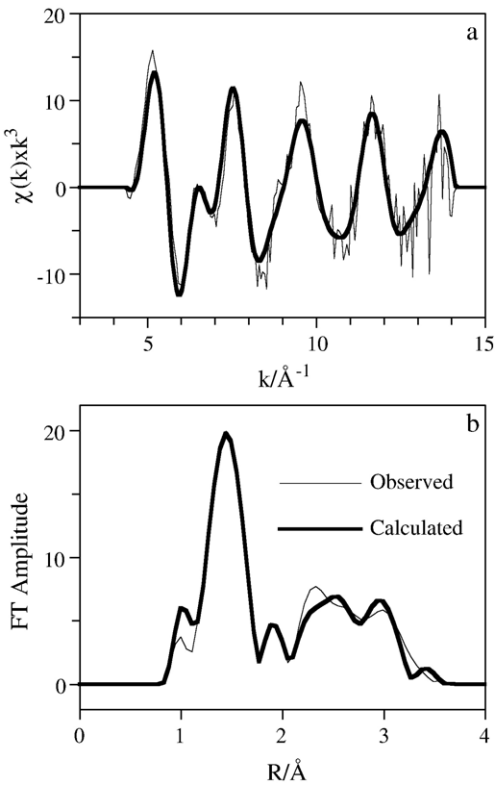

Fig. 4. Observed (raw) and calculated Ti K-edge (a) EXAFS and (b) FT EXAFS spectra of anhydrous forsterite containing 0.35 wt% TiO_2. Details of the model are given in Table 1.

Table 1
EXAFS shell model used to fit the data in Fig. 4

Element	*n**	Å	σ^2	n_{DFT}	$Å_{DFT}$
1st shell					
O	4.5	1.804(3)	0.001(1)	4	1.823
2nd shell					
Mg	3	2.831(5)	0.005(1)	3	2.837
3rd shell					
O	1	3.20(5)	0.020(7)	1	3.194
4th shell					
Mg	6	3.318(5)	0.006(1)	6	3.351
5th shell					
O	2	3.40(12)	0.021(−)	2	3.366
6th shell					
O	4	3.500(22)	0.021(−)	4	3.468
7th shell					
Si	2	3.700(27)	0.023(4)	2	3.686

For the element comprising each shell the number (*n*), the average distance from a central Ti atom (Å), and Debye-Waller factor (σ_2) are given. n_{DFT} and $Å_{DFT}$ are the number and distances calculated by DFT for the Ti defect site. The errors in the first shell were estimated from the result of various models. The remaining errors, arising from noise in the experimental data, were calculated by the Monte Carlo method.

Notes:

Scale factor (S_0^2)	0.97.
Goodness-of-fit parameter or residual (*R*)	18%.
k range $Å^{-1}$	4.5–14.0.
FT range	1.0–3.5.
Debye–Waller restraints	$\sigma^2<0.02$ {0.01}.
Debye–Waller constraints	$\sigma_5^2=\sigma_6^2$.

*n contstrained to n_{DFT} for all but 1st shell

Table 2
Total formation energies of the Ti bearing supercells calculated using the SIESTA methodology and solution enthalpies for reactions (1), (2) or (3)

Products of solution reaction	Total energy of defective supercell (eV)	Solution energy (eV)
$Ti_{Si}^{\times}+SiO_2$	−63967.17	0.98
$\{V_{Mg1}Ti_{Mg1}\}^{\times}+2MgO$	−62026.20	2.47
$\{V_{Mg1}Ti_{Mg2a}\}^{\times}+2MgO$	−62026.56	2.10
$\{V_{Mg1}Ti_{Mg2b}\}^{\times}+2MgO$	−62026.21	2.46
$\{V_{Mg1}Ti_{Mg2c}\}^{\times}+2MgO$	−62026.22	2.45
$\{V_{Mg2}Ti_{Mg1a}\}^{\times}+2MgO$	−62024.55	2.11
$\{V_{Mg2}Ti_{Mg1b}\}^{\times}+2MgO$	−62024.58	2.08
$\{V_{Mg2}Ti_{Mg1c}\}^{\times}+2MgO$	−62024.91	1.75
$\{V_{Mg2}Ti_{Mg2a}\}^{\times}+2MgO$	−62024.86	1.87
$\{V_{Mg2}Ti_{Mg2b}\}^{\times}+2MgO$	−62024.89	1.84
$\{Ti_{Mg1}Mg_{Sia}\}^{\times}+Si_2O$	−63965.49	2.73
$\{Ti_{Mg1}Mg_{Sib}\}^{\times}+Si_2O$	−63963.97	4.25
$\{Ti_{Mg2}Mg_{Sia}\}^{\times}+Si_2O$	−63964.68	3.54
$\{Ti_{Mg2}Mg_{Sib}\}^{\times}+Si_2O$	−63964.73	3.49
$\{Ti_{Mg2}Mg_{Sic}\}^{\times}+Si_2O$	−63964.20	3.97
$\{Ti_{Mg2}Mg_{Sid}\}^{\times}+Si_2O$	−63965.32	2.90

can occupy an M1 site sharing either a single O3 with the vacant site (configuration a), a single O1 (configuration b), or an octahedral edge terminated by O2 and O3 (configuration c). When the Ti ion occupies a M2 site, there are two possibilities, both of which involve sharing an O3 (there are two distinct pairs of O3 surrounding M2). These two configurations can be distinguished because one is in the layer above the vacant site (configuration a) and the other is in the layer below (configuration b). For Ti adjacent to a vacant M1 site there are four inequivalent ways to arrange the Ti ion, three involving an adjacent M2 site and one an adjacent M1, which shares an O1–O2 octahedral edge forming the chains of occupied octahedra parallel to c. The three ways involving M2 sites can be distinguished on the basis of which O sites are shared between the two octahedra. In the first case the M1 vacancy and the Ti-bearing octahedra share an O3–O2 edge (configuration a), in the second the two octahedra share only a single vertex O3 (configuration b), and in the third they share only a vertex O1 (configuration c).

Table 3
Total formation energies of quartz, rutile, MgO and forsterite calculated using the SIESTA methodology

	Formation energy (eV p.f.u.)
SiO_2 (quartz)	−982.77
TiO_2 (rutile)	−1641.39
MgO (periclase)	−1461.10
Mg_2SiO_4 (forsterite)	−3905.55

Table 4
Defect energies (eV) for cation vacancies and Ti substitution in forsterite calculated using the embedded cluster method

Method	$Ti_{M1}^{\cdot\cdot}$	$V_{Si}^{\cdot\cdot\cdot\cdot}$	Ti_{Si}^{x}	$V_{M1}^{\cdot\cdot}$	Reaction energy (reaction 4)
HF/6–31G// HF/6–31G	−61.06	108.58	11.90	25.83	−9.97
HF/6–31+G*// HF/6–31G	−60.99	111.87	14.49	24.94	−11.45
HF/6–31+G*// HF/6–31+G*	−61.12	–	–	24.97	–
PW91/6–31G// PW91/6–31G	−69.61	110.66	5.64	27.13	−8.28
PW91/6–31+G*// PW91/6–31G	−68.58	112.32	8.22	25.73	−9.79
PW91/6–31+G*// PW91/6–31+G*	−68.68	–	–	25.76	–

The energies are reported with respect to the perfect crystal and isolated ions and they vary with the method and basis set, represented by the standard nomenclature for calculations using the GAUSSIAN code. (The symbols before the double slash denote the method and basis set used for the calculation of the energy of the system and those after the double slash denote the method and basis set used for geometry optimisation. For example PW91/6–31+G*//PW91/6–31G represents a calculation where the geometry was optimised using a 6–31G basis with the PW91 DFT functional and the energy was then calculated using additional polarisation and disperse Gaussian functions. HF stands for the Hartree–Fock method.).

Similar considerations can be used for the coupled substitution of Mg on a Si site adjacent to Ti on a Mg site. In the case where the Ti occupies the M1 site there are four adjacent Si sites, two of which share an O1–O3 edge with the M1 site (configuration a) while the other two just share a vertex O2 (configuration b). For the case of Ti on an M2 site there are five adjacent Si sites. Three of these (configurations a, c and d) lie on the mirror plane passing through the M2 site while the fourth and fifth are symmetrically equivalent (configuration b). The Ti site shares a single O1 with the Si site in configuration a, a single O3 in configuration b, a single O2 in configuration c, and an O3–O3 edge with the Si site in configuration d.

The total energies of the 16 supercells described above are given in Table 2. When combined with the energies of the oxides, given in Table 3, the solution energies can be found. These are the enthalpy changes at zero Kelvin and zero pressure, neglecting the zero point energy, for the following reactions, written in Kröger–Vink notation:for the direct substitution of Ti on the Si site,

$$TiO_2 + Si_{Si}^{\times} \rightarrow SiO_2 + Ti_{Si}^{\times} \quad (1)$$

for the substitution of Ti on a Mg site charge balanced by the formation of a Mg vacancy,

$$TiO_2 + Mg_{M1}^{\times} + Mg_{M2}^{\times} \rightarrow 2MgO + \{V_{M1b}Ti_{M2}\}^{\times} \quad (2)$$

and for the coupled substitution,

$$TiO_2 + Si_{Si}^{\times} + Mg_{M2}^{\times} \rightarrow SiO_2 + \{Mg_{Si}Ti_{M2}\}^{\times} \quad (3)$$

For the three possible reactions the solution energies are given in Table 2. These energies can be directly compared in order to predict the thermodynamically preferred solution mechanism. This is simply the lowest energy reaction, which is found to be the direct substitution of Ti onto the Si site (reaction (1)).

Defect energies calculated using the embedded cluster method are defined with respect to the perfect crystal and isolated ions. For example, the defect energy of a vacancy is the sum of the energy of a nanocluster with an ion removed and the energy of the isolated ion minus the energy of the equivalent cluster without the defect. In the embedded cluster method there are additional contributions arising from the polarisation of the infinite dielectric continuum and the deviation of the electrostatic potential inside the nanocluster from that in the equivalent perfect crystal. The calculated defect energies are given in Table 4 with the individual contributions listed in the supplementary information.

These calculated defect energies can be used to predict if Ti substitutes onto a Mg or Si site by calculating the enthalpy change associated with the reaction:

$$Ti_{M1} + V_{Si}^{''''} \rightarrow Ti_{Si}^{\times} + V_{M1}^{''} \quad (4)$$

All methods predict that this reaction is exothermic with a change in the total energy of the crystal of −9.79 eV if the PW91 functional is used and −11.45 eV with the Hartree–Fock approximation. This indicates that the defect with Ti on the Si site is more stable than when Ti is on the Mg site.

Both sets of calculations also yield the structure of the defect formed by incorporation of Ti. This can be examined to extract calculated bond lengths which are given in Table 5 for a range of substitution mechanisms. In all cases where Ti(IV) substitutes onto the Si site the O ions move outwards and the Ti–O bonds are longer than the Si–O bonds in bulk olivine. The average bond lengths expand from 1.6 Å in bulk olivine to 1.8 Å around the Ti defect. Conversely, when Ti occupies either of the Mg sites the site contracts to give Ti–O bonds of ~2.0 Å.

4. Discussion

In Fig. 2 the results of the present study are referenced to the fields defined by the work of Farges et al. (1996). The pre-edge intensity of $Ni_{2.7}Ti_{0.7}O_4$ determined here is 0.82 compared to the literature value of 0.94. The difference is consistent with the decrease in intensity expected for the lower energy resolution of this work (1.8 eV) compared to that of Farges et al. (1.2 eV) which used Si(311) and Si(220) monochromators. In general, the comparison of intensity data between studies must be done with caution. However, the results for the standard compounds reported here are sufficient to discriminate clearly between Ti coordination environments in a way similar to that described by Farges et al. (1996). The energy of the intensity maximum is not affected by the experimental resolution. The points in Fig. 2 for Ti in anhydrous forsterite clearly indicate [4]-fold or tetrahedral coordination. The difference in resolution would only serve to increase the pre-edge intensity of this sample relative to the reference domains. The point for hydrous forsterite synthesised at 25 kbar indicates [6]-fold or octahedral Ti coordination. The 15 kbar hydrous sample appears to contain a mixture of $^{[4]}$Ti and $^{[6]}$Ti with 80–90% $^{[6]}$Ti.

Due to the polarisation of the excitation source the intensity of XANES features may vary with crystallographic orientation for non-cubic minerals such as

Table 5
Calculated Ti–O bond lengths (Å) from the periodic DFT and embedded cluster calculations

	Periodic DFT			Embedded cluster density functional theory)		Embedded cluster (Hartree–Fock)	
	$Ti_{Si}^{\times}$	$\{V_{Mg1}Ti_{Mg2a}\}^{\times}$	$\{Ti_{Mg1}Mg_{Sia}\}^{\times}$	$Ti_{Si}^{\times}$	$Ti_{M1}^{\bullet\bullet}$	$Ti_{Si}^{\times}$	$Ti_{M1}^{\bullet\bullet}$
Ti–O1	1.839	2.041	2.119, 1.964	1.852	1.979	1.833	1.964
Ti–O2	1.807	1.961	2.096, 2.077	1.797	1.997	1.786	1.961
Ti–O3a	1.820	1.967	2.191, 1.814	1.820	2.021	1.794	1.998
Ti–O3b	1.819	1.977					
Ti–O3c		2.062					
Ti–O3d		2.091					
Average	1.82	2.01	2.06	1.82	2.00	1.80	1.97

The average bond length takes account of the multiplicity of some of the bonds, there are two of each bond length for the embedded cluster calculations around the M1 site, and two Ti–O3 lengths for the Si centred site.

forsterite. Given the size of the incident beam (3 × 1 mm on the sample), the grain size of the anhydrous forsterite (50 μm), and the fact that the crystals were grown from powder in the absence of any applied stress, the experiment should sample a large number of randomly oriented grains and thus effectively correspond to the analysis of a powder. In the case of the hydrous samples, the XANES spectra were collected from only six crystals. Thus it is possible that the intensity of the pre-edge feature may be affected by the poor statistical sampling of the crystallographic orientation. Nevertheless, the randomisation is likely to be sufficient for the intensity to be correct, at least to first order. Further, the internal consistency of the various samples with reference to the mixing line suggests that any preferred orientation is not significant.

It should be noted that while the pre-edge energy and intensity of the 15 kbar sample can be reasonably simulated by a mixture of the anhydrous and 25 kbar hydrous spectra (see mixing trend in Fig. 2), the pre-edge can not be reproduced using the spectra for anhydrous forsterite and Ti-clinohumite. This suggests that Ti-clinohumite is not an exact structural analogue for the OH-coupled substitution of Ti in olivine, as might be expected given that its hydrated planar structure is very different to the hydrated point defect in forsterite identified by infrared spectroscopy (Berry et al., 2005).

The Ti–O bond length of 1.804 ± 0.003 Å found by modelling the EXAFS spectra of anhydrous forsterite is similar to that of $^{[4]}$Ti in β-Ba_2TiO_4 (1.808 Å) and $Ni_{2.6}Ti_{0.7}O_4$ (1.835 Å) but significantly smaller than for $^{[6]}$Ti in rutile (1.96 Å) or Ti-clinohumite (2.085 Å). While this strongly suggests that Ti is tetrahedrally coordinated, it is not an unambiguous result due to the unknown nature of the lattice distortion about the defect site. The EXAFS bond length is, however, in excellent agreement with the computational value of 1.8 Å for Ti on the Si site, but quite distinct from that calculated for Ti on a Mg site (2.0 Å). The expansion of the forsterite lattice that would occur due to Ti substituting for Si is consistent with the observed systematic increase in unit cell volume with increasing Ti content (Hermann et al., 2005).

The results of both first principles computational approaches indicate that it is energetically favourable for Ti to substitute for Si rather than Mg in forsterite. The reason for this is likely to be the high energetic cost of introducing a second defect for charge balance. It is important to realise that the reaction energies calculated from the embedded cluster method cannot be directly compared with the solution energies calculated using periodic DFT, but that both approaches yield the same conclusion. In addition to giving the lowest energy substitution mechanism in forsterite without experimental input, both methods yield a prediction for the structure of the defects. A critical test is to see if the predicted structure is consistent with the available experimental data. The calculations find that Ti will be tetrahedrally co-ordinated with an average Ti–O bond length of 1.8 Å, in excellent agreement with that found from the EXAFS. Irrespective of the method used, the Ti–O2 bond length is predicted to be shorter than the Ti–O3 bonds which, in turn, are predicted to be shorter than the Ti–O1 bond. It is often found that bond lengths calculated within the GGA are about 1% longer then the experimental determination. Conversely, the Hartree–Fock approximation tends to result in equilibrium bond lengths that are shorter than that found experimentally. The computational approach employed here is limited to the consideration of pure forsterite with a low concentration of Ti as the only impurity. Increasing the Ti concentration to the point where defects may cluster has not been considered.

Taken together (i) the energy and intensity of the $1s \rightarrow 3d$ pre-edge feature in the XANES spectrum, (ii) the determination by DFT that the direct substitution of Ti for Si is the defect with the lowest energy, and (iii) the agreement between the Ti–O bond length found by EXAFS and that determined computationally, provide unambiguous evidence that Ti occupies the Si site in anydrous forsterite.

The solubility of Ti as a $Mg_2^{[4]}TiO_4$ component in forsterite has been determined experimentally (Hermann et al., 2005). However, the Ti content of many natural samples exceeds the predicted saturation level. This has been interpreted to indicate a second mechanism of Ti incorporation, and in particular one associated with hydration. The mineral Ti-clinohumite comprises olivine-like units interleaved with Ti-rich hydrated layers, the formula of which can be written as $Mg^{[6]}TiO_2(OH)_2$. Dehydration of these Ti-clinohumite layers is a likely mechanism for producing olivine containing oriented ilmenite ($MgTiO_3$) rods (Risold et al., 2001). Isolated Ti-clinohumite-like planar defects may, however, persist beyond the stability field of the humite minerals. These defects, identified by TEM, exhibit hydroxyl region infrared bands identical to pure Ti-clinohumite (Hermann et al., 2007). There is also strong evidence to suggest that Ti and water may be associated at a point defect (Berry et al., 2005, Walker et al., in press). This defect has a similar but distinct infrared signature characterised by intense bands at 3572 and 3524 cm^{-1}, which occur in essentially all samples of mantle olivine from spinel peridotite xenoliths. Further, these bands

can only be reproduced experimentally in the presence of Ti (Berry et al., 2005).

Thus, while there is a single mode of Ti incorporation in anhydrous forsterite, in natural olivines there are three possible ways in which Ti may substitute in the presence of hydroxyl i.e. at non-negligible fugacity of H_2O. These are Ti substitution for Si, Ti-clinohumite-like planar defects, and Ti-clinohumite-like point defects. In a similar computational study we have investigated the effect of Ti on H incorporation and determined the energy and structure of the hydrated point defect associated with Ti (Walker et al., in press). It was found that H acts to stabilise Si vacancies so that instead of $^{[4]}$Ti on a Si site, the most stable configuration is for $^{[6]}$Ti on an M1 site sharing an edge with a vacant Si site. The two O around the Si site that do not form Ti–O bonds instead bond with two H to form OH groups and stabilise the under-bonded O. This defect is lower in energy than any other hydrated defect (e.g. Mg or Si vacancies) coexisting with Ti on the Si site. This effectively means that if anhydrous forsterite containing Ti is hydrated, the defect structure will rearrange, with Ti moving from the Si site to a Mg site, creating the Ti–OH point defect. The XANES spectra of the hydrous samples reported here confirm this change in Ti coordination (Fig. 3). Further, there is an increase in $^{[6]}$Ti relative to $^{[4]}$Ti with increasing pressure (from 15 to 25 kbar). This is expected, at constant temperature, due to both the negative effect of pressure on the stability of the $Mg_2^{[4]}TiO_4$ component (Hermann et al., 2005) and the increased stabilisation of $^{[6]}$Ti in a Ti-clinohumite-like defect as the stability field of the Ti-clinohumite mineral phase is approached. The infrared spectrum of this sample is typical of that attributed to the Ti point defect (see Fig. 1e of Berry et al., 2005). The H_2O content determined from the spectrum is 150 ppm by weight, with a probable uncertainty from all sources, including calibration, of about 50%. This is in good agreement with the value of 200±20 ppm that would be expected for water incorporation as a $Mg^{[6]}TiO_2(OH)_2$ defect, given a TiO_2 content of 0.11±0.01 wt% and that 80±10% of the Ti is present at this site. It is important to note that because of the various modes of Ti incorporation in olivine no correlation between Ti and water content need be expected.

In terms of water incorporation in mantle olivine this study demonstrates that there is a change in Ti coordination between anhydrous and hydrous olivine, which provides a hydration mechanism. This site change creates a hydrated Si vacancy, thus producing an infrared signature that is similar to, but nevertheless distinguishable from, that of samples synthesised at low silica activity in Ti-free systems (Matveev et al., 2001; Lemaire et al., 2004). It has been shown that close to the Ti-clinohumite stability field water may be incorporated in olivine as Ti-clinohumite-like planar defects (Hermann et al., 2007). At conditions removed from the stability field, such as the high temperatures and comparatively low pressures characteristic of spinel peridotite, the planar defects do not occur and instead Ti-clinohumite-like point defects are the primary mode of water incorporation. Analogously, the hydrated Si vacancy experimentally produced in the absence of Ti may be conveniently termed an OH-clinohumite-like point defect. The infrared signature characteristic of this defect dominates the spectra of synthetic samples buffered with pyroxene at high pressures (>5 GPa; Kohlstedt et al., 1996), even though at low pressures the defect only occurs when buffered with magnesiowüstite. This signature also appears to occur only in high pressure natural samples (Mosenfelder et al., 2006). We suggest that this defect is stabilised in the mantle at pressures approaching the OH-clinohumite stability field.

Acknowledgements

We thank the Australian Research Council for financial support. Part of this work was performed at the Australian National Beamline Facility with support from the Australian Synchrotron Research Program, which is funded by the Commonwealth of Australia under the Major National Research Facilities Program. J.D.G. thanks the Government of Western Australia for support under the Premiers Research Fellowship program. High performance computing facilities were provided by the Australian Partnership for Advanced Computing and the Centre for Advanced Data Inference.

Appendix A. Supplementary data

Supplementary data associated with this article can be found, in the online version, at 10.1016/j.chemgeo.2007.03.010.

References

Berry, A.J., Hermann, J., O'Neill, H.St.C., Foran, G.J., 2005. Fingerprinting the water site in mantle olivine. Geology 33, 869–872.

Braithwaite, J.S., Sushko, P.V., Wright, K., Catlow, C.R.A., 2002. Hydrogen defects in Forsterite: a test case for the embedded cluster method. Journal of Chemical Physics 116, 2628–2635.

Braithwaite, J.S., Wright, K., Catlow, C.R.A., 2003. A theoretical study of the energetics and IR frequencies of hydroxyl defects in forsterite. Journal of Geophysical Research Solid Earth 108. doi:10.1029/2002JB002126 (art. num. 2284).

de Leon, J.M., Rehr, J.J., Zabinsky, S.I., Albers, R.C., 1991. Ab initio curved-wave X-ray absorption fine structure. Physical Review B 44, 4146–4156.

Dingwell, D.B., Paris, E., Seifert, F., Mottana, A., Romano, C., 1994. X-ray absorption study of Ti-bearing silicate glasses. Physics and Chemistry of Minerals 21, 501–509.

Dobrzhinetskaya, L., Green, H.W., Wang, S., 1996. Alpe Arami: a peridotite massif from depths of more than 300 km. Science 271, 1841–1845.

Ellis, P.J., Freeman, H.C., 1995. XFIT — an interactive EXAFS analysis program. Journal of Synchrotron Radiation 2, 190–195.

Farges, F., Brown Jr., G.E., 1997. Coordination chemistry of titanium(IV) in silicate glasses and melts: IV. XANES studies of synthetic and natural volcanic glasses and tektites at ambient temperature and pressure. Geochimica et Cosmochimica Acta 61, 1863–1870.

Farges, F., Brown Jr., G.E., Rehr, J.J., 1996. Coordination chemistry of Ti (IV) in silicate glasses and melts: I. XAFS study of titanium coordination in oxide model compounds. Geochimica et Cosmochimica Acta 60, 3023–3038.

Frisch, M.J., Trucks, G.W., Schlegel, H.B., Scuseria, G.E., Robb, M.A., Cheeseman, J.R., Zakrzewski, V.G., Montgomery, J.A., Stratmann, R.E., Burant, J.C., Dapprich, S., Millam, J.M., Daniels, A.D., Kudin, K.N., Strain, M.C., Farkas, O., Tomasi, J., Barone, V., Cossi, M., Cammi, R., Mennucci, B., Pomelli, C., Adamo, C., Clifford, S., Ochterski, J., Petersson, G.A., Ayala, P.Y., Cui, Q., Morokuma, K., Malick, D.K., Rabuck, A.D., Raghavachari, K., Foresman, J.B., Cioslowski, J., Ortiz, J.V., Baboul, A.G., Stefanov, B.B., Liu, G., Liashenko, A., Piskorz, P., Komaromi, I., Gomperts, R., Martin, R.L., Fox, D.J., Keith, T., Al-Laham, M.A., Peng, C.Y., Nanayakkara, A., Gonzalez, C., Challacombe, M., Gill, P.M.W., Johnson, B.G., Chen, W., Wong, M.W., Andres, J.L., Head-Gordon, M., Replogle, E.S., Pople, J.A., 1998. Gaussian 98 (Revision A.7). Gaussian Inc., Pittsburg.

Green, H.W., Dobrzhinetskaya, L., Riggs, E.M., Zhen-Ming, J., 1997. Alpe Arami: a peridotite massif from the mantle transition zone. Tectonphysics 279, 1–21.

Hartman, P., 1969. Can Ti^{4+} replace Si^{4+} in silicates? Mineralogical Magazine 37, 366–369.

Hermann, J., O'Neill, H.St.C., Berry, A.J., 2005. Titanium solubility in olivine in the system TiO_2–MgO–SiO_2: no evidence for an ultra-deep origin of Ti-bearing olivines. Contributions to Mineralogy and Petrology 148, 746–760.

Hermann, J., Fitz Gerald, J., Malaspina, N., Berry, A.J., Scambelluri, M., 2007. OH-bearing planar defects in olivine produced by the breakdown of Ti-rich humite minerals from Dabie Shan (China). Contributions to Mineralogy and Petrology 153, 417–428.

Hohenberg, P., Kohn, W., 1964. Inhomogeneous electron gas. Physical Review 136, 864–871.

Junquera, J., Paz, O., Sánchez-Portal, D., Artacho, E., 2001. Numerical atomic orbitals for linear-scaling calculations. Physical Review B 64 (art. num. 235111).

Kitamura, M., Kondoh, S., Morimoto, N., Miller, G.H., Rossman, G.R., Putnis, A., 1987. Planar OH-bearing defects in mantle olivine. Nature 328, 143–145.

Kohlstedt, D.L., Keppler, H., Rubie, D.C., 1996. Solubility of water in the α, β and γ phases of (Mg, Fe)$_2SiO_4$. Contributions to Mineralogy and Petrology 123, 345–357.

Kohn, W., Sham, L.J., 1965. Self-consistent equations including exchange and correlation effects. Physical Review 140, 1133–1138.

Krause, M.O., Oliver, J.H., 1979. Natural widths of atomic K and L levels, Kα X-ray lines and several KLL Auger lines. Journal of Physical and Chemical Reference Data 8, 329–338.

Lager, G.A., Armbruster, T., Ross, F.K., Rotella, F.J., Jorgensen, J.D., 1981. Neutron powder diffraction study of defect spinel structures: tetrahedrally coordinated Ti^{4+} in $Ni_{2.62}Ti_{0.69}O_4$ and $Ni_{2.42}Ti_{0.74}Si_{0.05}O_4$. Journal of Applied Crystallography 14, 261–264.

Lemaire, C., Kohn, S.C., Brooker, R.A., 2004. The effect of silica activity on the incorporation mechanism of water in synthetic forsterite: a polarised infrared spectroscopic study. Contributions to Mineralogy and Petrology 147, 48–57.

Matveev, S., O'Neill, H.S.C., Ballhaus, C., Taylor, W.R., Green, D.H., 2001. Effect of silica activity on OH–IR spectra of olivine: implications for low-$a$$SiO_2$ mantle metasomatism. Journal of Petrology 42, 721–729.

Mosenfelder, J.L., Sharp, T.G., Asimow, P.D., Rossman, G.R., 2006. Hydrogen incorporation in natural mantle olivines. In: Jacobsen, S.D., van der Lee, S. (Eds.), Earth's Deep Water Cycle. Geophysical Monograph Series, vol. 168. AGU Geophysical Monograph, pp. 45–56.

O'Neill, H.St.C., Navrotsky, A., 1983. Simple spinels — crystallographic parameters, cation radii, lattice energies, and cation distribution. American Mineralogist 68, 181–194.

Paris, E., Dingwell, D.B., Seifert, F.A., Mottana, A., Romano, C., 1994. Pressure-induced coordination change of Ti in silicate glass: a XANES study. Physics and Chemistry of Minerals 21, 510–515.

Perdew, J.P., 1991. In: Zesche, P., Eschrig, H. (Eds.), Electronic Structure of Solids'91. Akaemie Verlag, Berlin, p. 11.

Perdew, J.P., Wang, Y., 1992. Accurate and simple analytic representation of the electron-gas correlation energy. Physical Review B 45, 13244–13249.

Perdew, J.P., Burke, K., Emzerhof, M., 1996. Generalized gradient approximation made simple. Physical Review Letters 77, 3865–3868.

Risold, A.C., Trommsdorff, V., Grobéty, B., 2001. Genesis of ilmenite rods and palisades along humite-type defects in olivine from Alpe Arami. Contributions to Mineralogy and Petrology 140, 619–628.

Soler, J.M., Artacho, E., Gale, J.D., García, A., Junquera, J., Ordejón, P., Sánchez-Portal, D., 2002. The SIESTA method for ab initio order-N materials simulation. Journal of Physics. Condensed Matter 14, 2745–2776.

Sushko, P.V., Shluger, A.L., Baetzold, R.C., Catlow, C.R.A., 2000a. Embedded cluster calculations of metal complex impurity defects: properties of the iron cyanide in NaCl. Journal of Physics. Condensed Matter 12, 8257–8266.

Sushko, P.V., Shluger, A.L., Catlow, C.R.A., 2000b. Relative energies of surface and defect states: ab initio calculations for the MgO (001) surface. Surface Science 450, 153–170.

Troullier, N., Martins, J.L., 1991. Efficient pseudopotentials for plane-wave calculations. Physical Review B 43, 1993–2006.

Walker, A.M., Hermann, J., Berry, A.J., O'Neill, H.St.C., 2007. Three water sites in upper mantle olivine and the role of titanium in the water weakening mechanism. Journal of Geophysical Research 112. doi:10.1029/2006JB004620.

Waychunas, G.A., 1987. Synchrotron radiation XANES spectroscopy of Ti in minerals: effects of Ti bonding distances, Ti valence, and site geometry on absorption edge structure. American Mineralogist 72, 89–101.